Available online at www.sciencedirect.com
SCIENCE DIRECT®
Journal of Physiology - Paris 97 (2003) 237–252
Journal of Physiology Paris
www.elsevier.com/locate/jphysparis

Large-scale modeling of the primary visual cortex: influence of cortical architecture upon neuronal response

David McLaughlin *, Robert Shapley, Michael Shelley

Courant Institute of Mathematical Sciences, Center for Neural Science, New York University, 251 Mercer Street, New York, NY 10012, USA

Abstract

A large-scale computational model of a local patch of input layer $4C\alpha$ of the primary visual cortex (V1) of the macaque monkey, together with a coarse-grained reduction of the model, are used to understand potential effects of cortical architecture upon neuronal performance. Both the large-scale point neuron model and its asymptotic reduction are described. The work focuses upon orientation preference and selectivity, and upon the spatial distribution of neuronal responses across the cortical layer. Emphasis is given to the role of cortical architecture (the geometry of synaptic connectivity, of the ordered and disordered structure of input feature maps, and of their interplay) as mechanisms underlying cortical responses within the model. Specifically: (i) Distinct characteristics of model neuronal responses (firing rates and orientation selectivity) as they depend upon the neuron's location within the cortical layer relative to the pinwheel centers of the map of orientation preference; (ii) A time independent (DC) elevation in cortico-cortical conductances within the model, in contrast to a "push–pull" antagonism between excitation and inhibition; (iii) The use of asymptotic analysis to unveil mechanisms which underly these performances of the model; (iv) A discussion of emerging experimental data. The work illustrates that large-scale scientific computation—coupled together with analytical reduction, mathematical analysis, and experimental data, can provide significant understanding and intuition about the possible mechanisms of cortical response. It also illustrates that the idealization which is a necessary part of theoretical modeling can outline in sharp relief the consequences of differing alternative interpretations and mechanisms—with final arbiter being a body of experimental evidence whose measurements address the consequences of these analyses.

Keywords: Visual cortex; Dynamics; Architecture; Orientation tuning

1. Introduction

A common view held within theoretical neural science is that numerical simulations of large-scale neuronal networks are both too complex, and too simple, to provide much real insight into the neural mechanisms of cortical response. Too complex because of the large number of parameters that must be fixed in a reasonably sophisticated model, and too simple because the brain is so complex on so many scales. While both of these statements are undoubtedly true—there are many parameters to be fixed and the brain is exceedingly complex—we have not found their apparent corollary to be so. We have found instead that when coupled together with analytical reduction and mathematical analysis, and with a close eye to experimental data to help fix parameters and bound the possibilities of cortical activity, that such an approach can provide significant understanding and intuition about the possible mechanisms of cortical response. Further, the idealization that is a necessary part of theoretical modeling has the added (and sometimes overlooked) advantage of outlining in sharp relief the consequences of differing alternative interpretations. The final arbiter is of course a body of experimental evidence whose measurements address the consequences of these analyses. We hope to illustrate our view through a central point of our modeling: To understand how response in the visual cortex is shaped by its geometry of connectivity, the ordered and disordered structure of its input maps, and their interaction.

The primary visual cortex of the macaque monkey is a layered structure, for which we [32] have developed a

* Corresponding author. Tel.: +1-212-998-3077; fax: +1-212-995-4121.
E-mail address: dmac@cims.nyu.edu (D. McLaughlin).

0928-4257/$ - see front matter © 2003 Elsevier Ltd. All rights reserved.
doi:10.1016/j.jphysparis.2003.09.019

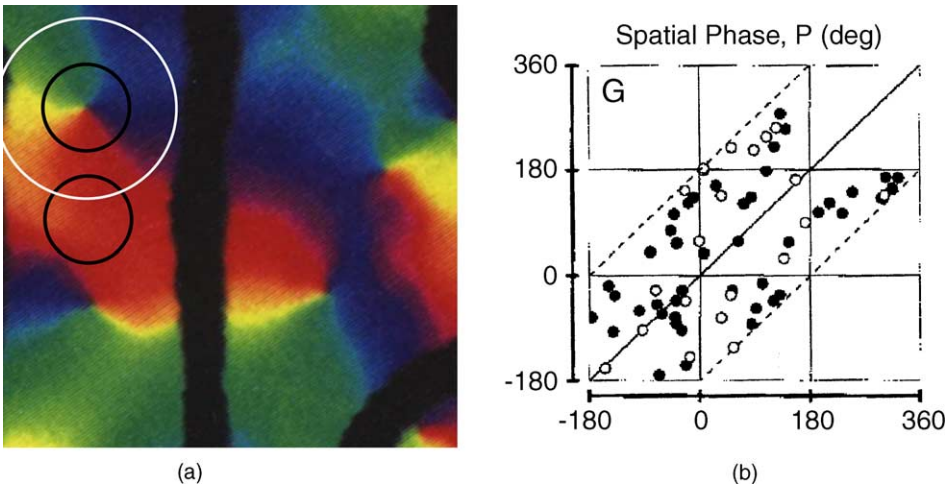

Fig. 1. (a) From Blasdel [6], a detail from an optical imaging of the orientation mapping across the superficial layers of macaque V1, over an area $\sim$1 mm^2. The image shows four orientation hypercolumns with pinwheel centers. The superimposed black circles show the estimated length-scale of monosynaptic inhibition in the local connections of layer 4$C\alpha$, while the white circle is that for excitation. (b) From DeAngelis et al. [17], a comparison of preferred spatial phase for pairs of nearby cortical neurons.

large-scale computational model of a set of orientation hypercolumns within its input layer 4$C\alpha$. This is a detailed point-neuron model, whose construction and performance are both highly constrained by experimental observations. With this large-scale model, we have investigated potential effects of cortical architecture upon neuronal performance. In part, we have focused upon the features of *orientation preference* (as discovered by Hubel and Wiesel [25,26], the increased firing rate of cortical neurons when a simple visual stimulus, say a bar or grating, is set at a particular angle) and *orientation selectivity* (how well that preference is expressed). In McLaughlin et al. [32] we show that the model qualitatively captures the observed selectivity, diversity, and dynamics of orientation tuning of neurons in the input layer, under visual stimulation by both drifting and randomly flashed gratings [36,37]; in Wielaard et al. [47] we show also that remarkably for a nonlinear network, the model captures the well known and important linear dependence of Simple cells upon visual stimuli, in a manner consistent with both extracellular [16] and intracellular [19,27] measurements; and in Shelley et al. [40] we show that cortical activity places our computational model cortex in a regime of large conductances, primarily inhibitory, consistent with recent intracellular measurements [2,9,24].

By "cortical architecture" we mean the spatial footprints of synaptic connectivity within the cortex, together with the structure of "maps" of features (angle, phase, ...) of visual stimuli. Within the cortex, feature maps can be *ordered* or *disordered*. Orientation preference, with its beautiful pinwheel patterns revealed by optical imaging experiments (see Fig. 1(a)) [6–8,31], provides an example of an ordered map which regularly tiles the cortical layer. On the other hand, the map of spatial phase preference is apparently disordered, or distributed randomly [17] from a broad distribution (see Fig. 1(b)). The interplay of these two distinct types of feature maps, with each other, and with the spatial length-scales set by the synaptic footprints, can shape neuronal response. We will use large-scale computational modeling, together with an analytical reduction to coarse-grained representations developed by Shelley and McLaughlin [39], to understand the consequences of this interplay. Thus, we describe one illustrative example of the qualitative insight which can be obtained from a combination of large-scale modeling with asymptotic reduction.

2. Materials and methods

2.1. The large-scale model

Our initial model, described in [32,47], is a large-scale, detailed cortical model of a small local patch (1 mm^2) of input layer 4$C\alpha$ for V1 of macaque monkey—a patch containing four "orientation hypercolumns" with four pinwheel centers. This input layer receives visual input from the retina through the lateral geniculate nucleus (LGN). Our model consists of a two-dimensional lattice of 128^2 coupled I&F neurons, of which 75% are excitatory and 25% are inhibitory. Imaging, anatomical, and physiological measurements constrain the representation of the model's neuronal components as well as their coupling architecture; moreover, the model network's performance with respect to steady-state and dynamical orientation selectivity, and the response properties of

Simple cells, is consistent qualitatively with laboratory observations.

Distinctive features of our model include:

- A local lateral connectivity that is *nonspecific* and *isotropic*, with lateral monosynaptic inhibition acting at shorter length-scales than excitation [13,14,20,30].
- An ordered map for orientation preference of cortical neurons laid out as pinwheel patterns across the model's cortical surface, as revealed by optical imaging experiments [6–8,31,34] of preference in the upper layers of V1. Orientation preference is conferred on the model's cortical cells from the convergence of output from many LGN cells [1,35], laid out as segregated subregions of On- and Off-center cells.
- A disordered map of spatial phase preference, coming with a broad distribution [17]. Again, the convergent input from LGN cells sets a spatial phase preference which varies widely from cortical neuron to cortical neuron.
- A predominance of cortico-cortical inhibition.

The equations of the model: The model itself consists of equations for the membrane potentials of excitatory (inhibitory) neurons, denoted by v_{E}^j (v_{I}^j):

$$\frac{\mathrm{d}v_{\mathrm{P}}^j}{\mathrm{d}t} = -g_{\mathrm{L}} v_{\mathrm{P}}^j - g_{\mathrm{PE}}^j(t)[v_{\mathrm{P}}^j - V_{\mathrm{E}}] - g_{\mathrm{PI}}^j(t)[v_{\mathrm{P}}^j - V_{\mathrm{I}}], \quad \mathrm{P} = \mathrm{E}, \mathrm{I} \tag{1}$$

whose evolution determines the mth spike-and-reset time, t_m^j of, this jth model neuron, defined by

$$v_{\mathrm{P}}^j(t_m^j) = 1; \quad v_{\mathrm{P}}^j(t_m^j + 0^+) = 0. \tag{2}$$

Here the superscript $j = (j_1, j_2)$ indexes the spatial location of the neuron within the cortical layer. In these equations, we have normalized the potentials, making them dimensionless quantities. In this normalization process, we begin with commonly accepted dimensional values for cellular biophysical parameters: the capacitance $C = 10^{-6}$ F cm^{-2}, the leakage conductance $g_{\mathrm{L}} = 50 \times 10^{-6}$ Ω^{-1} cm^{-2}, the leakage reversal potential $V_{\mathrm{R}} = -70$ mV, the excitatory reversal potential $V_{\mathrm{E}} = 0$ mV, the inhibitory reversal potential $V_{\mathrm{I}} = -80$ mV [28], the spiking threshold $\bar{v} = -55$ mV, and the reset potential set at the leakage reversal potential, -70 mV. Then the transformation $v \to (v - V_{\mathrm{R}})/(\bar{v} - V_{\mathrm{R}})$ sets the spiking threshold to unity, the reset potential to zero, $V_{\mathrm{E}} = 14/3$, and $V_{\mathrm{I}} = -2/3$. Within this normalization, the potentials range over $-2/3 \leqslant v_{\mathrm{E}}^j,\ v_{\mathrm{I}}^j \leqslant 1$. To convert back to dimensional quantities, insert the dimensionless v into the formula $v_{mV} = (\bar{v} - V_{\mathrm{R}})v + V_{\mathrm{R}}$.

Conductances: First, we note that the capacitance C does not appear in Eq. (1), as all conductances have been rescaled as rates, with units of s^{-1}, through division by C. Throughout we will use conductances normalized as rates in order to emphasize the time-scales which they represent. For example, the leakage conductance $g_{\mathrm{L}} = 50$ s^{-1} produces a leakage time-scale of $\tau_{\mathrm{L}} = g_{\mathrm{L}}^{-1} = 1/(50\ \mathrm{s}^{-1}) = 20$ ms. True conductances are obtained by multiplication by $C = 10^{-6}$ F cm^{-2}; for example, $g_{\mathrm{L}} = 50\ \mathrm{s}^{-1} \times 10^{-6}\ \mathrm{F\,cm}^{-2} = 50$ nS.

The time-dependent conductances arise from the input forcing (through the LGN) and from noise to the layer, as well as from the cortical network activity of the excitatory and inhibitory populations. They have the form:

$$\begin{aligned} g_{\mathrm{EE}}^j(t) &= F_{\mathrm{EE}}(t) + S_{\mathrm{EE}} \sum_k a_{j-k} \sum_l G_{\mathrm{E}}(t - t_l^k), \\ g_{\mathrm{EI}}^j(t) &= f_{\mathrm{EI}}^0(t) + S_{\mathrm{EI}} \sum_k b_{j-k} \sum_l G_{\mathrm{I}}(t - T_l^k), \end{aligned} \tag{3}$$

with similar expressions for g_{IE}^j and g_{II}^j, where

$$F_{\mathrm{PE}}(t) = g_{\mathrm{lgn}}^j(t) + f_{\mathrm{PE}}^0(t), \quad \mathrm{P} = \mathrm{E}, \mathrm{I}.$$

Here t_l^k (T_l^k) denotes the time of the lth spike of the kth excitatory (inhibitory) neuron. Note that g_{EE} (g_{EI}) is the conductance driven by excitatory (inhibitory) network activity, and that the first "E" labels the postsynaptic target as an excitatory cell. The conductances $f_{\mathrm{PP}'}^0(t)$ are stochastic and represent synaptic activity from other areas of the brain.

The conductance $g_{\mathrm{lgn}}^j(t)$ denotes the drive from the LGN by which the visual signal (standing, drifting, or random gratings) is relayed through convergent LGN neurons to the jth cortical neuron. For *drifting gratings*, the visual stimulus on the "screen" has intensity pattern $I = I(x, t; \theta, \phi, k, \omega, I_0, \epsilon)$ given by

$$I = I_0[1 + \epsilon \cos[(\vec{k} \cdot \vec{x} - \omega t + \phi)]], \tag{4}$$

where $\vec{k} = k(\cos\theta, \sin\theta)$. Here $\theta \in [-\pi, \pi)$ denotes the orientation of the sinusoidal pattern on the screen, $\phi \in [0, 2\pi)$ denotes its spatial phase, $\omega \geqslant 0$ its frequency, I_0 its intensity, and ϵ its "contrast".

Spatial patterns of orientation preference: Optical imaging [6–8,31] reveals "pinwheel" patterns of orientation preference in the superficial layers 2/3 of the cortex (see Fig. 1(a)); neurons of like-orientation preference reside along the same radial spoke of a pinwheel, with the preferred angle sweeping through 180° as the center of the pinwheel is encircled. We assume that there are pinwheel patterns in layer 4$C\alpha$, parallel to those in layers 2/3.

This tiling of the cortical layer by pinwheel patterns of orientation preference, as well as the random map of spatial phase preference (see Fig. 1(b)), are conferred upon the model through the LGN drive $g_{\mathrm{lgn}}^j(t)$. The total input into the jth cortical neuron arrives from N ($\simeq$20) LGN cells:

$$g_{\mathrm{lgn}}^j(t) = \sum_{i=1}^{N} \left\{ g_0^j + \int_0^t \mathrm{d}s \int \mathrm{d}^2x G_{\mathrm{lgn}}(t-s) A(\vec{x}_i^j - \vec{x}) I(\vec{x}, s) \right\}^+. \tag{5}$$

Here $\{R\}^+ = R$ if $R > 0$; $\{R\}^+ = 0$ if $R \leqslant 0$; g_0^j represents the maintained (background) activity of the LGN neurons feeding into the jth cortical neuron, in the absence of visual stimulation. The temporal kernel $G_{\rm lgn}(t)$ and spatial kernel $A(\vec{x})$ of an LGN cell are chosen to agree with experimental measurements [5,38]. The orientation preference map is hard-wired into the cortical model, through the orientation preference of each group of LGN cells that converge onto each cortical cell [35]. That is, the spatial arrangement of LGN cell receptive field centers, $\vec{x}_l^j$, confers an orientation preference (in pinwheel patterns) on the input to each cortical cell in the model. Additionally, the center of each cortical cell's receptive field (created through the aggregate LGN input) is randomized, which confers a preferred spatial phase on the LGN input of each cortical cell that is distributed randomly [17], with a broad distribution.

The temporal kernels $G_\sigma(t)$ model the time course of synaptic conductance changes in response to arriving spikes from the other neurons, which introduces the time-scale $\tau_{\rm syn} = 4$–6 ms according to the formula

$$G_{\rm lgn}(t) = c_0 t^5[\exp(-t/\tau_0) - c_1 \exp(-t/\tau_1)], \quad \text{where}$$
$$\tau_0 = 3 \text{ ms}, \ \tau_1 = 5 \text{ ms}.$$

The constant c_1 is determined so that the kernel $G(t)$ integrates to zero, as is approximately the case for LGN neurons in the magnocellular pathway [5,38].

The kernel $A(\vec{y})$ is of the form

$$A(\vec{y}) = \pm\left\{ \frac{a}{\pi\sigma_a^2} \exp\left[-|\vec{y}/\sigma_a|^2 \right] - \frac{b}{\pi\sigma_b^2} \exp\left[-|\vec{y}/\sigma_b|^2 \right] \right\},$$

$\sigma_a = 1.25k_0^{-1}$, $\sigma_b = 1.75k_0^{-1}$, $a = 1$, $b = 0.74$, with k_0 the preferred spatial frequency, and where + represents an "on-center," and − an "off-center" LGN cell.

The Gaussian kernels $(a, b, \ldots)$ represent the spatial coupling between neurons, with the spatial length-scale of excitation (radius 200 μm) exceeding that of inhibition (radius 100 μm). This local (within one hypercolumn) spatial coupling architecture is spatially isotropic, which reflects our understanding of cortical anatomy. We do not make the further assumption that these local synaptic connections selectively couple specific feature preferences—such as iso-orientation, like (or anti) spatial phase. This local isotropy is consistent with local anatomy, although the anatomy of long range (over several hypercolumns) is observed to selectively couple iso-orientation patches. For example, in the superficial layers the longer range lateral connections are known to be spatially heterogeneous [10,12,49], with connection patterns coupling neurons of "like-orientation" preferences in a distinctive nonisotropic fashion. (See [11] for theoretical modeling of this nonisotropic architecture.)

The computational model's behavior depends on the choice of the cortico-cortical synaptic coupling coefficients: $S_{\rm EE}$, $S_{\rm EI}$, $S_{\rm IE}$, $S_{\rm II}$. All cortical kernels have been normalized to unit area. Hence, these coupling coefficients represent the strength of interaction, and are treated as adjustable parameters in the model. In the numerical experiments reported here, the strength matrix ($S_{\rm EE}$, $S_{\rm EI}$, $S_{\rm IE}$, $S_{\rm II}$) was set to be (0.8, 9.4, 1.5, 9.4). This matrix means cortical inhibition dominates in that inhibitory neurons have much stronger coupling to all other cortical neurons than do excitatory neurons. The matrix given here generates simple cells that have the orientation selectivity, and the magnitude and dynamics of response, seen in physiological experiments [32].

2.1.1. The numerical method for the large-scale network

There are two main elements to address in the numerical simulation of the model network, as given by Eq. (1). The first is the evaluation of the cortico-cortical conductances, as given by Eq. (3), that account for the consequences of spiking activity within the network. For the simulations presented here, we exploit the fact that the connectivity is nonspecific and isotropic, that is, that the connection kernels $a, b, \ldots$, depend only upon $j - k$, and that we have chosen the neurons to lie on a spatial lattice. Hence we need to evaluate discrete convolutions of the form:

$$g^j = \sum_k A_{j-k} B_k(t).$$

We evaluate this efficiently in $O(N \log N)$ operations, where N is the number of neurons, using the discrete convolution theorem, and the fast Fourier transform algorithm. This is a "presynaptic" method. Each presynaptic neuron (labeled k) has an amount of conductance to distribute, i.e. $B_k(t) = \sum_l G(t - t_l^k)$, to all the other postsynaptic neurons, with a weighting of A_{j-k}.

The second main issue is the temporal integration of the potential equation (1). There are various sources of error. Foremost is that resulting from the resetting of the potential v^j to zero following a spike (Eq. (2)). Generically the potential will cross spiking threshold between time-steps. If the potential is simply reset to zero at the end of that time-step, then the error introduced reduces the accuracy of the time-integration to first order, that is $O(\Delta t)$, regardless of the order of the time-stepping algorithm. To achieve a given level of accuracy then can necessitate using an unnecessarily small time-step. However, if account is made of the spike-time being between time-steps, and an appropriate correction made to the reset potential at the end of the time-step, then accuracy can be restored to the integration (see [23,41]). In the simulations reported here we use a second-order Runge–Kutta method, developed in Shelley and Tao [41], where appropriate correction for spiking is made. This correction restores high accuracy to the integration, at essentially no extra computational cost. Another source of error is due to the onset of conductance changes induced by arriving spikes, as

modeled by the kernel $G_{\rm lgn}(t)$. A typical α-function rises linearly from zero, while the kernel we use here rises more smoothly (like t^5 locally). As is analyzed in Shelley and Tao, the smoothness of the onset dictates the maximal order possible for an integration scheme. In later work we have employed a fourth-order variant of the Runge–Kutta scheme to achieve high accuracy at moderate cost, as well as developed efficient schemes that avoid constraining the point-neurons to a lattice [45].

2.2. The coarse-grained reduction

While amenable to large-scale simulation and post-processing of the simulational data, the full network equations (1) are typically too complex to study analytically. A reduced representation which is more amenable to analytical investigation and is easier to study numerically is desirable. To obtain a reduced representation, in Shelley and McLaughlin [39] we reduce the full network to a spatially coarse-grained network expressed in terms of average firing rates over coarse-grained cells (termed a "CG-cell"; see the schematic in Fig. 2). As it is an asymptotic approximation which introduces no additional phenomelogical parameters, this mathematical reduction provides a valid approximate representation of the full neuronal network. This reduced representation retains dependence upon spatial location within the two-dimensional cortical layer, with cortical interactions relative to cortical location within the orientation hypercolumn.

Cortical maps such as orientation preference are arranged in regular patterns which tile cortical layers (Fig. 1(a)). Thus, we partition the two-dimensional cortical layer into CG-cells, each containing many neurons, yet small enough in spatial extent that ordered mapped properties are roughly uniform within the CG-cell. This is in opposition to disordered quantities such as preferred spatial phase ϕ, that are apparently distributed randomly from cortical neuron to cortical neuron (Fig. 1(b)). Accordingly, we will also assume that within each CG-cell there are sufficiently many neurons that the distributions of disordered quantities, such as preferred spatial phase, are well sampled.

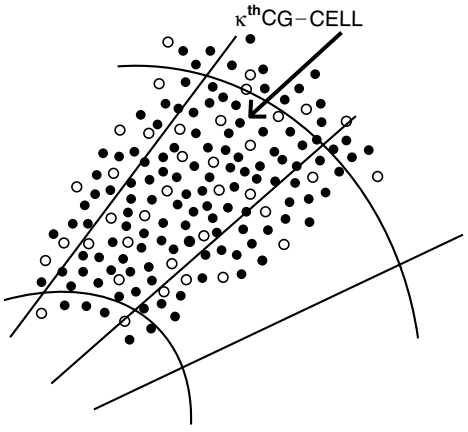

Fig. 2. A schematic illustrating the tiling of the cortical surface into coarse-grained cells.

The asymptotic methods are founded upon the separation of spatial length-scales associated with this coarse-grained tiling, and upon a separation of time-scales: there are three important time-scales in Eq. (1): the LGN response time $\tau_{\rm lgn} = {\rm O}(10^2$ ms); a shorter time-scale of the cortical-cortical interaction times (and the noise, presumably synaptically mediated) $\tau_{\rm s} = {\rm O}(4$ ms) [3,22]; and the shortest, the response time of neurons within an active network: $\tau_{\rm g} = {\rm O}(2$ ms) [40,47]. We emphasize that the latter is a property of network activity. While the separation of $\tau_{\rm s}$ and $\tau_{\rm g}$ is only a factor of 2, when the network is under stimulation, our numerical simulations [40] show that this is sufficient to cause cortical neurons to respond with near instantaneity to presynaptic cortical input. In the asymptotic reduction, we assume and use the separation of time-scales, $\tau_{\rm g}/\tau_{\rm syn} \ll 1$, to help relate conductances to firing rates.

The separation of spatial scales allows a "Monte-Carlo" approximation by integrals of the summations in the conductances, Eq. (3). For example,

$$\begin{aligned}\tilde{g}_{\rm EE}(\mathbf{x},t;\langle m_{\rm E}\rangle_\phi) &= S_{\rm EE}\sum_{k,l} K^{\rm EE}_{j-k} G_{\rm E}(t-t^k_l)\\ &\simeq S_{\rm EE}\int {\rm d}^2\mathbf{x}'\int_{-\infty}^{t} {\rm d}s\, K_{\rm EE}(\mathbf{x}-\mathbf{x}')\\ &\quad\times G_{\rm E}(t-s)\langle m_{\rm E}\rangle_\phi(\mathbf{x}',s)\\ &\equiv (S_{\rm EE}K_{\rm EE} * G_{\rm E} * \langle m_{\rm E}\rangle_\phi)(\mathbf{x},t),\end{aligned}$$

where

$$\langle m_{\rm E}\rangle_\phi(\mathbf{x},t) \equiv \int m_{\rm E}(\mathbf{x},t;\phi)\rho(\phi)\,{\rm d}\phi,$$

$\rho(\phi)$ denotes the probability density of the spatial phase preference ϕ, and where $\mathbf{x}$ denotes the spatial location of the CG-cell.

Together with this coarse-graining, the separation of time-scales $\tau_{\rm g} \ll \tau_{\rm syn}$ permits Eq. (1) to be integrated asymptotically to yield a *closed* set of equations for the average excitatory and inhibitory firing rates $m_{\rm P}(\mathbf{x},t;\phi)$, P = E, I, of neurons in the CG-cell at $\mathbf{x}$:

$$m_{\rm P}(\mathbf{x},t;\phi) = \mathcal{N}_{\rm P}(\mathbf{x},t;\langle m_{\rm E}\rangle_\phi,\langle m_{\rm I}\rangle_\phi,\phi) \tag{6}$$

for P = E and I. Here,

$$\begin{aligned}&\mathcal{N}_{\rm P}(\mathbf{x},t;\langle m_{\rm E}\rangle_\phi,\langle m_{\rm I}\rangle_\phi,\phi)\\ &\quad= -g_{\rm T,P}\Big/\log\left(\frac{\{I_{\rm D,P}-g_{\rm T,P}\}^+}{g_{\rm T,P}+\{I_{\rm D,P}-g_{\rm T,P}\}^+}\right)\end{aligned} \tag{7}$$

where

$$g_{\mathrm{T,P}} \equiv g_{\mathrm{R}} + g_{\mathrm{lgn}}(\mathbf{x}, t; \phi) + \sum_{\mathrm{P}'} \left(\tilde{g}_{\mathrm{PP}'}(\mathbf{x}, t; \langle m_{\mathrm{P}'} \rangle_{\phi}) + \bar{f}_{\mathrm{P}'} \right) \tag{8}$$

is the total conductance, and

$$I_{\mathrm{D,P}} \equiv V_{\mathrm{E}}\, g_{\mathrm{lgn}}(\mathbf{x}, t; \phi) + \sum_{\mathrm{P}'} V_{\mathrm{P}'} \left(\tilde{g}_{\mathrm{PP}'}(\mathbf{x}, t; \langle m_{\mathrm{P}'} \rangle_{\phi}) + \bar{f}_{\mathrm{P}'} \right) \tag{9}$$

is the so-called "difference current" [47], as it arises as the difference of excitatory and inhibitory synaptic currents. The thresholding $\{I_{\mathrm{D,P}} - g_{\mathrm{T,P}}\}^{+}$ in Eq. (7) is taken to imply that $\mathcal{N} = 0$ if $I_{\mathrm{D,P}} - g_{\mathrm{T,P}} \leqslant 0$. This latter quantity is the "threshold membrane current", obtained by setting $v^j = 1$ in Eq. (1), and its positivity is a necessary condition for cell spiking.

The coarse-grained equation (6) can be averaged with respect to ϕ to yield closed space- and time-dependent equations for the phase-averaged firing rates:

$$\langle m_{\mathrm{P}} \rangle_{\phi}(\mathbf{x}, t) = \left\langle \mathcal{N}_{\mathrm{P}}(\mathbf{x}, t; \langle m_{\mathrm{E}} \rangle_{\phi}, \langle m_{\mathrm{I}} \rangle_{\phi}, \phi) \right\rangle_{\phi}. \tag{10}$$

This system can be solved for phase-averaged quantities directly through Eq. (10), whose solution can then be used to reconstruct phase-dependent quantities through Eq. (6).

Other sources of noise, such as background noisy conductances with fluctuations on the synaptic timescale, can be incorporated with similar methods to those described here for the random distribution of spatial phase preferences [39]. One should note too that the coarse-grained asymptotics is a large N limit; hence, it will not capture finite size effects (which one does see in numerical simulations of the I&F system, and most certainly in in vivo response).

2.2.1. The numerical method for the CG network

In comparison to the point-neuron simulations, simulating a CG network is far simpler. With appropriate choices of temporal kernels $G_{\mathrm{E,I}}(t)$, Eq. (10) can be rewritten as a set of differential equations in time for the evolution of $\langle m_{\mathrm{P}} \rangle_{\phi}$. As there is now no spike and reset mechanism, standard time-integrators can be used. FFTs are still used to rapidly evaluate the spatial convolutions, though now at a coarser spatial description than for the point-neuron simulations. Details can be found in Shelley and McLaughlin [39].

3. Results

3.1. Results from numerical simulations of the full network

An important feature of large-scale cortical modeling is the ease with which one can obtain spatial distributions of populations of neurons. That is, in addition to pointwise measurements of single neuronal properties (such as firing rates, orientation selectivity, and time traces of membrane potentials and conductances), one can display and analyze the spatial distribution of the population across the cortical layer.

For example, in Fig. 3 we show the spatial distribution of two response properties across the model's four hypercolumns. The left panel shows the spatial distribution of time-averaged firing rates of excitatory cells in the simple cell network described above, driven by a drifting grating visual stimulus. The right panel shows the circular variance of the orientation tuning curves, which provides one measure of the neurons' selectivity as orientation detectors, and is defined by

$$\mathrm{CV}[m^j] \equiv 1 - \frac{\int m^j(\theta) \exp 2i\theta \, \mathrm{d}\theta}{\int m^j(\theta) \, \mathrm{d}\theta}, \tag{11}$$

where $m^j(\theta)$ denotes the (time-averaged) firing rate of the jth cortical neuron, as a function of the orientation θ of the grating pattern. This measure satisfies $0 \leqslant \mathrm{CV}[m^j] \leqslant 1$, with sharply tuned neurons possessing a CV near 0 and broadly tuned near 1. Notice from Fig. 3 that the neurons with the highest firing rates are located near the pinwheel centers, and that (for this network of simple cells) the most sharply tuned neurons are also located near the pinwheel centers.

The cortical activity, and thus the "cortical operating point" is perhaps best described by the conductances. Fig. 4(a) shows the spatial distribution of the temporal averages of the total conductance of the excitatory neurons $g_{\mathrm{T,E}}$, while Fig. 4(b) shows the standard deviation of the temporal fluctuations of these total conductances—again for drifting grating stimulation at high contrast. In Fig. 4(a) for the average conductance, there is rather flat uniform behavior in regions far from the

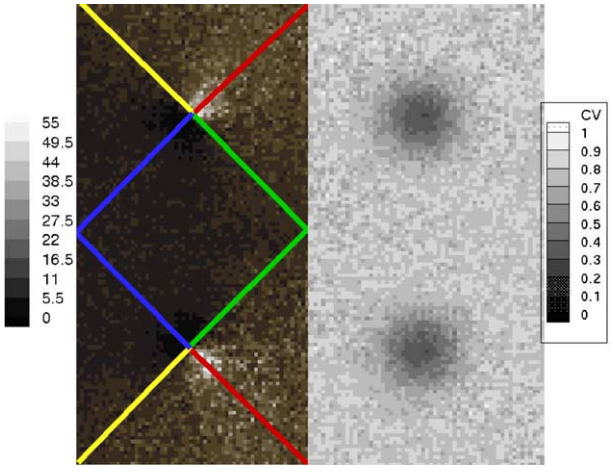

Fig. 3. From the point-neuron network simulations, the spatial distribution of time-averaged firing rates (left panel), and of circular variance (right panel), across the model cortical surface (~1 mm^2).

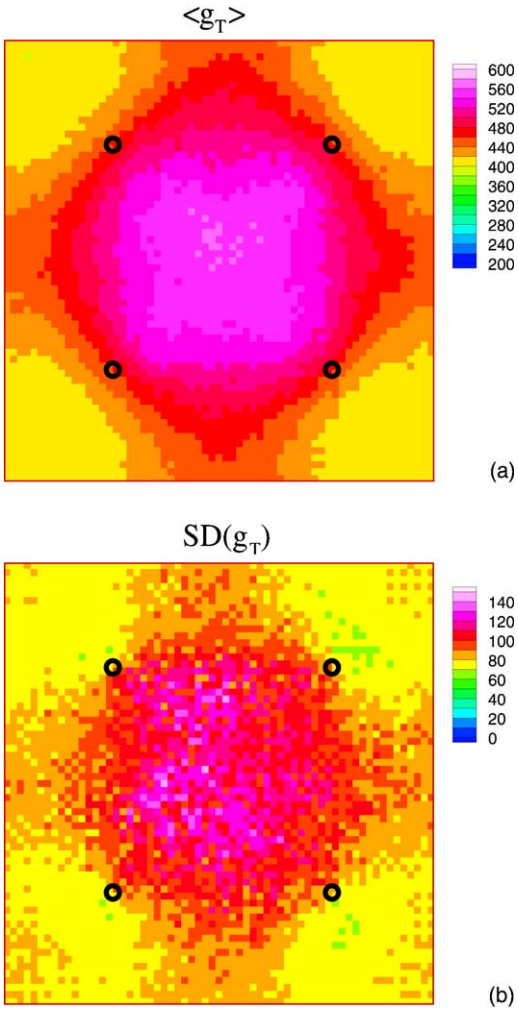

Fig. 4. The spatial distribution of the neurons' total conductance across the model cortical surface. Here, unlike the previous figure, the stimulated orientation columns lie in the center of the figures. (a) temporal averages; (b) standard deviations of the temporal fluctuations.

pinwheel centers. For example, in the "center" region of preferred orientation, centered at (1,1) in Fig. 4(a), note the uniformly high conductance, and the uniformly low conductance in the "corner" region of orthogonal to preferred orientation (centered at (0,0) in Fig. 4(a)). Note too that even regions of nonpreferred orientation have conductances well above background values (400 s^{-1}, as compared with background values of 230 s^{-1}). Near the pinwheel centers, the average conductance changes rather rapidly in space, over distances of 100 μm, as set by the axonal arbors of the inhibitory neurons. The fluctuations (Fig. 4(b)) are significantly larger far from pinwheels than near. Fig. 4(a) and (b) show that the modulation of the total conductance (between its large value for stimulation at preferred orientation and its smaller response at stimulation orthogonal to preferred) is greater for far neurons than near. Indeed, at *preferred orientation*:

$$g_{\mathrm{T,near}} = 475 \pm 90\ \mathrm{s}^{-1}, \quad g_{\mathrm{T,far}} = 550 \pm 100\ \mathrm{s}^{-1};$$

and at *orthogonal to preferred*:

$$g_{\mathrm{T,near}} = 460 \pm 70\ \mathrm{s}^{-1}, \quad g_{\mathrm{T,far}} = 400 \pm 80\ \mathrm{s}^{-1}.$$

Different stimuli, such as drifting vs. randomly flashed gratings, create very different and distinct conductance maps on the cortex. For drifting grating stimulation, there is not uniform conductance across the entire cortical layer, but rather, different spatial regions within the layer have different values of the conductance, with the conductance changing most rapidly near pinwheel centers. In contrast, for randomly flashed grating stimuli, the temporal mean and standard deviation of the temporal fluctuations of the conductance are distributed relatively uniformly throughout the entire layer (not shown).

Numerical simulation also enables one to extract components from the model's response—components which are very informative about cortical mechanisms, yet are often difficult to extract from experimental measurements. For example, in Fig. 5 we show the five components of the total conductance (the excitatory LGN, noise, and cortico-cortical conductances; and the inhibitory noise and cortico-cortical conductances) for a sample excitatory neuron in the simple cell model. A high contrast stimulus is switched on at $t = 1$ s, before which the model cortex is in a background state in the

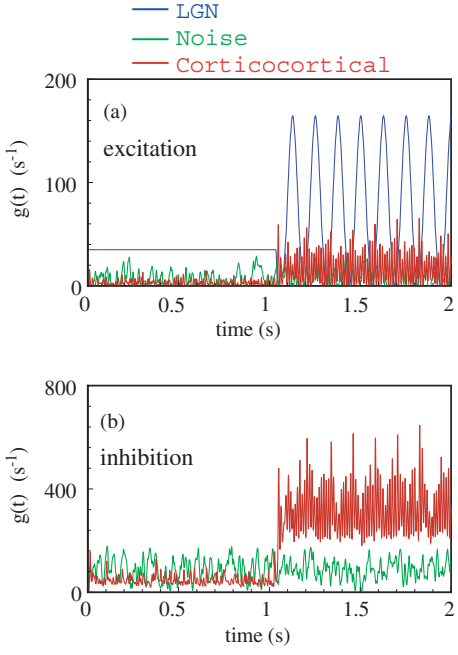

Fig. 5. The five components of the total conductance for a model cortical neuron—without visual stimulation and for randomly flashed stimuli (switched on after one second). (a) Excitatory: LGN (blue), cortical interaction from layer 4$C\alpha$ (red) and noise (green). (b) Inhibitory: cortical interaction from layer 4$C\alpha$ (red) and noise (green). Notice the difference in the vertical scales for (a) and (b).

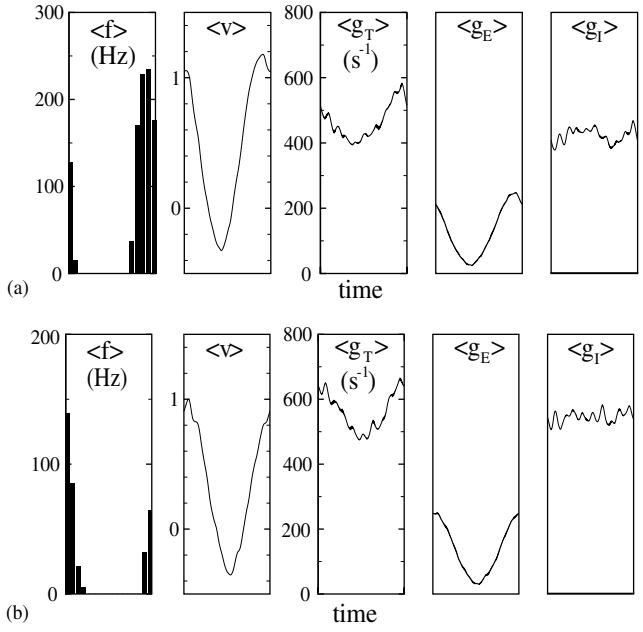

Fig. 6. Responses to drifting gratings. This stimulus was a drifting sinusoidal grating at optimal spatial frequency and orientation, at a drift rate of 8 Hz and 100% contrast. From left to right, the panels shown are cycle averaged spike rate, blocked membrane potential, total conductance, excitatory conductance, and inhibitory conductance. (a) A model neuron near a pinwheel center. (b) A model neuron far from a pinwheel center. Note the difference in scales for firing rate.

absence of visual stimulation. Note the balances in this simple cell network—with cortical excitation dominated by the LGN, yet with cortico-cortical inhibition dominating all conductances.

Fig. 6 provides a different view of these components, together with the firing rate and the (blocked to prohibit spiking) membrane potential for a sample neuron near a pinwheel center—cycle averaged relative to the period of the drifting grating stimulus. Note again the dominance of cortico-cortical inhibition. Also note that the cortico-cortical excitation and inhibition are near constant, with no temporal fluctuations on the time-scale of the sinusoidal grating. This elevated DC behavior of the cortico-cortical conductances is an important response property of our model cortex, which does not show cortico-cortical inhibition in "push–pull" antagonism with the LGN excitation.

Fig. 6(b) shows the same quantities as Fig. 6, but for a sample neuron far from pinwheel centers.

3.1.1. Summary of results from large-scale model

Sample network responses include: The large-scale model produces cortical maps with distinctive responses between neurons near and far from orientation pinwheel centers. The highest firing rates are found near. Simple cells are more selective for orientation near, while temporal fluctuations are more pronounced far. Cortico-cortical conductances are basically DC in time, with no temporal oscillations on the time-scale of the sinusoidal drifting grating. In the next section, we will use the coarse-grained network to identify and explain those mechanisms within the model which are responsible for these sample cortical responses.

3.2. Cortical mechanisms from coarse-grained representation

We begin our discussion of results for the reduced coarse-grained representation with the observation that, for drifting grating stimuli (Eq. (4)) with sufficiently high contrast, the LGN conductance g_{lgn} (see Eq. (5)) can be well approximated by the analytical expression

$$\begin{aligned} g_{\mathrm{lgn}}(\mathbf{x},t;\theta,\phi) &= g_{\mathrm{lgn}}\left(\Theta(\mathbf{x}),\frac{2\pi}{T}t-\phi;\theta\right) \\ &\simeq C\epsilon\left(1+\frac{1}{2}(1+\cos 2(\Theta(\mathbf{x})-\theta))\right. \\ &\quad \left.\times\sin\left(\frac{2\pi}{T}t-\phi\right)\right) \end{aligned} \tag{12}$$

where $T=2\pi/\omega$ is the temporal period of the stimulus, $\Theta(\mathbf{x})$ denotes the angle of orientation preference of neurons within the coarse-grained cell at cortical location $\mathbf{x}$, and $\phi\in[0,2\pi)$ denotes a random phase difference between the spatial phase of the grating and preferred spatial phase of the neurons within the coarse-grained cell $\mathbf{x}$. The constant $C\approx 80$. (Note that since g_{lgn} is π-periodic, this parameterization does not capture the direction of grating drift.) Also note that the linear growth of both mean and temporal modulation with contrast ϵ follows from the onset of strong rectification in Eq. (5). This parameterization captures neither low contrast behavior, where the temporal modulations occur against a fixed background mean, nor the saturation of individual LGN cells at high contrast. It does capture an important feature of the input from LGN to cortex [46]: because of the approximate axisymmetry of the receptive field of a single LGN cell, its time-averaged firing rate is independent of the orientation of the drifting grating. Hence, the sum of activities of many such cells, averaged over time, is likewise independent of stimulus orientation [43,46], or

$$\langle g_{\mathrm{lgn}}\rangle_{\mathrm{T}}=\bar{g}. \tag{13}$$

That is, the time-averaged LGN input is *independent* of stimulus orientation θ, information on which is only encoded in temporal modulations.

3.2.1. Cortico-cortical conductances are primarily DC

Since the forcing from the LGN is of the form $g_{\mathrm{lgn}}=g_{\mathrm{lgn}}(\Theta(\mathbf{x}),t-\frac{T}{2\pi}\phi;\theta)$, we look for solutions $m_{\mathrm{E,I}}$ to the coarse-grained Eq. (6) that reflect the structure of

this forcing, and are temporally periodic with arguments shifted relative to the preferred phase ϕ. That is,

$$m_{\mathrm{P}}(\mathbf{x},t;\theta,\phi)=\bar{m}_{\mathrm{P}}\left(\mathbf{x},\frac{2\pi}{T}t-\phi;\theta\right),\quad \mathrm{P}=\mathrm{E},\mathrm{I}. \tag{14}$$

As measured experimentally in [17], the distribution of spatial phase is broad. In the large-scale model, it is taken as a uniform distribution on $[0,2\pi)$, $\rho=1/2\pi$, in which case phase averages become temporal averages, that is $\langle\bar{m}_{\mathrm{P}}\rangle_{\phi}=\langle\bar{m}_{\mathrm{P}}\rangle_{\mathrm{T}}$. This temporal average is over T, the period of $\bar{m}$, and is obviously independent of time t. Further,

$$\begin{aligned}\int_{-\infty}^{t}\mathrm{d}s\,G_{\mathrm{P}}(t-s)\langle\bar{m}_{\mathrm{P}}\rangle_{\phi}(\mathbf{x},s)&=\int_{-\infty}^{t}\mathrm{d}s\,G_{\mathrm{P}}(t-s)\langle\bar{m}_{\mathrm{P}}\rangle_{\mathrm{T}}(\mathbf{x})\\&=\langle\bar{m}_{\mathrm{P}}\rangle_{\mathrm{T}}(\mathbf{x}),\end{aligned}$$

since G_{P} has been normalized to unit area. The cortico-cortical conductances then take the form

$$S_{\mathrm{PE}}K_{\mathrm{PE}}*\langle\bar{m}_{\mathrm{E}}\rangle_{\mathrm{T}}\quad\text{and}\quad S_{\mathrm{PI}}K_{\mathrm{PI}}*\langle\bar{m}_{\mathrm{I}}\rangle_{\mathrm{T}}, \tag{15}$$

i.e. are only spatial convolutions. The uniform distribution of random spatial phases has led to the result that, within the model, cortico-cortical conductances are *independent of time*. Hence, a temporally modulated "push–pull" antagonism between excitation and inhibition is not present in this model network.

3.2.2. Structure of the CG equations for drifting gratings

The coarse-grained Eq. (6) for drifting gratings now take the simplified form

$$\begin{aligned}\bar{m}_{\mathrm{P}}\left(\mathbf{x},\frac{2\pi}{T}t-\phi;\theta\right)&=\mathscr{N}_{\mathrm{P}}\left(\mathbf{x},\frac{2\pi}{T}t-\phi;\langle m_{\mathrm{E}}\rangle_{\mathrm{T}},\langle m_{\mathrm{I}}\rangle_{\mathrm{T}}\right)\\&=\overline{\mathscr{N}}_{\mathrm{P}}\left(g_{\mathrm{lgn}}\left(\Theta(\mathbf{x}),\frac{2\pi}{T}t-\phi;\theta\right),\right.\\&\qquad\left.S_{\mathrm{PP}'}K_{\mathrm{PP}'}*\langle\bar{m}_{\mathrm{P}'}\rangle_{\mathrm{T}}(\mathbf{x})\right),\end{aligned} \tag{16}$$

for P = E, I. Here $\overline{\mathscr{N}}_{\mathrm{P}}$ denotes the different labeling of the arguments of $\mathscr{N}_{\mathrm{P}}$. As the only time and phase dependence is through their difference, the phase average of Eq. (16) again converts to a time average, yielding two closed fixed-point equations for the time-averaged firing rates:

$$\langle\bar{m}_{\mathrm{P}}\rangle_{\mathrm{T}}(\mathbf{x})=\left\langle\overline{\mathscr{N}}_{\mathrm{P}}\left(g_{\mathrm{lgn}}(\Theta(\mathbf{x}),t;\theta),S_{\mathrm{PP}'}K_{\mathrm{PP}'}*\langle\bar{m}_{\mathrm{P}'}\rangle_{\mathrm{T}}(\mathbf{x})\right)\right\rangle_{\mathrm{T}}, \tag{17}$$

for P = E, I. Eq. (17) are a beautifully simplified and closed pair of fixed point equations for the temporally averaged firing rates. Solution of these time-independent equations allows for the reconstruction of time-dependent firing rates from Eq. (16).

3.2.3. Some numerical simulations of CG network

Fig. 7 shows the components of the conductances from the CG network, to be compared with Fig. 6 for the full large-scale point neuron network. Overall, it agrees quite well with the full point-neuron simulations in capturing the differences near and far from the pinwheel center. Notice too the absence of temporal modulations in the cortico-cortical conductances, as well as the dominance of inhibition.

For the CG network driven by drifting gratings, Fig. 8 shows the time-averaged firing rate, and CV, across

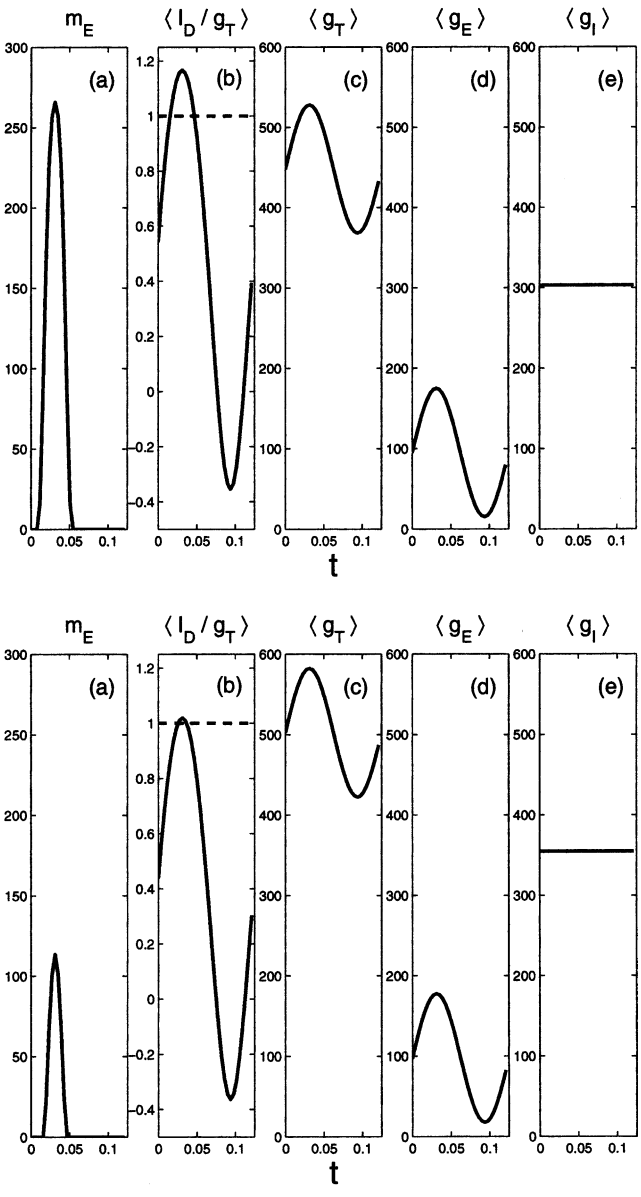

Fig. 7. From the full CG network: (a) The time-dependent firing rate $m_{\mathrm{E}}(t)$ over a stimulus cycle for CG-cells in Fig. 8 for drifting grating stimulus at full contrast ($\epsilon=1$), and at preferred orientation. (b) The expectation of the effective reversal potential $V_S(t)$. The dashed line is at the threshold to firing. (c,d,e) The expectations of g_{T}, g_{E}, and g_{I}, respectively. Cf. Fig. 6. Top: A CG-cell near a pinwheel center. Bottom: A CG-cell far from a pinwheel center.

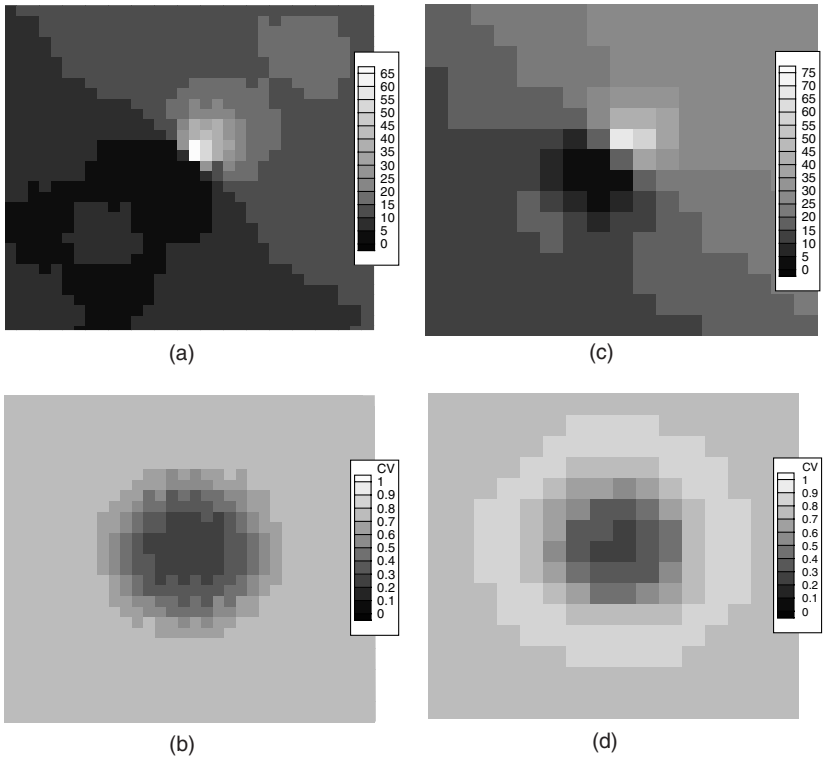

Fig. 8. From the full CG network: the distribution across the model cortex of time-averaged firing rates ((a) excitatory, (c) inhibitory), and of circular variance ((b) excitatory, (d) inhibitory). Cf. Fig. 3. Here, only one of the four orientation hypercolumns in the model is shown.

model cortical surface. This is to be compared with Fig. 3 for the full point neuron model. Fig. 8(a) shows the spatial distribution of time-averaged firing rates for excitatory CG-cells in the CG network, while Fig. 8(b) shows the associated circular variance of orientation selectivity. Again, cells with the highest firing rates are located near the pinwheel centers, and (for this network of simple cells) the most sharply tuned cells are also located near the pinwheel centers. Fig. 8(c) and (d) show these distributions for the inhibitory CG-cells.

This CG representation provides results in good agreement with the full large-scale point neuron model, and it does so with significant savings in numerical efficiency. For example, the CG maps of circular variance required (using a far from optimal relaxation algorithm) 2–3 h of CPU time on a single processor SGI (R10000 chip), versus 2–3 days on the same machine for the large-scale point neuron code. Clearly such CG representations may prove very useful as parameterizations for scale-up to more global cortical models.

3.3. Analytical understanding of cortical mechanisms

Numerical simulations from both the large-scale point neuron model and its coarse-grained reduction show distinct neuronal responses, depending upon the neuron's location relative to the orientation pinwheels which tile the cortical layer. The magnitude of firing rates, the degree of orientation selectivity (as captured by circular variance), and the amplitudes of temporal fluctuations all depend upon location within this tiling—as is particularly apparent in the cortical maps of Figs. 3 and 4, and is also captured in the CG representation (as in Fig. 8). Clearly, the mechanisms in the model which result in this spatial dependence must arise from the interaction of the regular map of orientation preference, the random map of spatial phase preference, the spatial scales of cortico-cortical synaptic interactions, and the dominance of cortico-cortical inhibition. In this section we show that the CG representation (Eqs. (16) and (17)) can be used to provide an analytical understanding of these mechanisms within the model cortical network. Here we will assume that the pinwheel structure fills the entire plane, with its pinwheel center at the origin.

3.3.1. Special cases of the CG equations

Eqs. (6) and (10) are the general form of the CG equations, with nonlinearity given by Eq. (7) (or its generalizations to include other effects, such as background noise—see Shelley and McLaughlin [39]). For simple analytical insight, it is best to use various simplifications, or models, or these equations. For the case of *drifting grating stimuli* these models take the form:

(I) The *thresholded-linear* equations, in which $\mathcal{N}_P$ in Eq. (7) is replaced by

$$\mathcal{N}_P = \{I_{D,P} - g_{T,P}\}^+ \tag{18}$$

where

$$I_{D,P} - g_{T,P} = f\left(\mathbf{x}, \frac{2\pi}{T}t - \phi\right) + C_{PE} \cdot K_{PE} * \langle m_E \rangle_T(\mathbf{x}) - C_{PI} \cdot K_{PI} * \langle m_I \rangle_T(\mathbf{x}),$$

and

$$f\left(\mathbf{x}, \frac{2\pi}{T}t - \phi\right) \equiv -g_R + (V_E - 1)g_{lgn}\left(\mathbf{x}, \frac{2\pi}{T}t - \phi\right)$$
$$C_{PE} \equiv (V_E - 1)S_{PE} \geqslant 0$$
$$C_{PI} \equiv (1 - V_I)S_{PI} \geqslant 0.$$

This is a useful model: first, it captures the nonlinearity of thresholding, while replacing the nonlinear argument with a linear one—the threshold membrane current. Second, it retains monotonic dependencies upon excitatory and inhibitory conductances. And third, it retains the proper requirement for threshold to firing, a positive threshold membrane current, $I_{D,P} > g_{T,P}$. Eq. (18) is very similar to the Wilson–Cowan mean-field models [48], though with the inclusion of phase-averaged arguments.

(II) *The far-field reduction*: Consider a single orientation hypercolumn filling the entire plane. Then far from a pinwheel center, g_{lgn} (at a given phase) will change very little over a coupling length-scale $L_{PP'}$ encoded in $K_{PP'}$. (This statement is especially relevant to the shorter inhibitory length-scales L_{PI}.) In this case, one can seek solutions $\langle m_P \rangle_\phi$ that likewise vary slowly over these length-scales, in which case

$$\tilde{g}_{PP'}(\mathbf{x}, t) \approx S_{PP'} \cdot \langle m \rangle_T(\mathbf{x}). \tag{19}$$

(This uses that $K_{PP'}$ has unit spatial integral.) Then Eq. (10), for example, will take the form of *spatially local* fixed point equations,

$$\left\langle m_P\left(\mathbf{x}, \frac{2\pi}{T}t - \phi\right)\right\rangle_T = \left\langle \mathcal{N}_P\left(\mathbf{x}, \frac{2\pi}{T}t - \phi; \langle m_E(\mathbf{x})\rangle_T, \langle m_I(\mathbf{x})\rangle_T\right)\right\rangle_T = \left\langle \overline{\mathcal{N}}_P\left(g_{lgn}\left(\Theta(\mathbf{x}), \frac{2\pi}{T}t - \phi; \theta\right); S_{PP'} \cdot \langle m_{P'}\rangle_T(\mathbf{x})\right)\right\rangle_T, \tag{20}$$

to be solved point-wise in $\mathbf{x}$. Note that if $g_{lgn} = g_{lgn}(\Theta, t; \phi)$, i.e. as with drifting grating stimuli, g_{lgn} depends spatially only on the hypercolumn angular coordinate, then the solutions $\langle m_P \rangle_T$ will also depend spatially only upon Θ.

(III) *The near-field model*: In the neighborhood of a pinwheel center, the synaptic sampling of cortical cells occurs at all angles around the pinwheel center. We model this by including an "angle" average in the synaptic contributions, i.e.,

$$\langle m_P \rangle_T(\Theta) = \left\langle \overline{\mathcal{N}}_P\left(g_{lgn}\left(\Theta, \frac{2\pi}{T}t - \phi\right); S_{PP'} \cdot \langle m_{P'}\rangle_{T,\Theta}\right)\right\rangle_T. \tag{21}$$

Here, we have assumed g_{lgn} depends spatially only on Θ, as would be the case for drifting grating stimuli. Obviously, this expression can be averaged once more with respect to Θ to yield a closed equation for $\langle m_P \rangle_{T,\Theta}$. This model is very similar to one studied by Ben-Yishai et al. [4], that they termed the "Hubel-Wiesel model with uniform cortical inhibition".

3.3.2. Mechanisms for cortical responses

To show that the coarse-grained representation unveils the mechanisms which underly the striking spatial distributions of the cortical responses, we model the cortical layer as a single orientation hypercolumn that fills the plane, with its pinwheel center at the origin. This is reasonable for the case at hand as the length-scale of monosynaptic inhibition, L_{PI}, lies below a hypercolumn width, as Fig. 1(a) well illustrates. Further, we consider as the simplest model the *thresholded-linear* CG equation (18):

$$\langle m_P \rangle_T(\mathbf{x}) = \langle \{I_{D,P}(\mathbf{x}, t) - g_{T,P}(\mathbf{x}, t)\}^+ \rangle_T = \left\langle \{f(\Theta(\mathbf{x}), t) + C_{PE} \cdot [K_{PE} * \langle m_E \rangle_T](\mathbf{x}) - C_{PI} \cdot [K_{PI} * \langle m_I \rangle_T](\mathbf{x})\}^+ \right\rangle_T \tag{22}$$

for $P = E, I$. Here it is worth recalling Eq. (13), which implies that $\langle f \rangle_T = \bar{f}$ is independent of Θ. This implies that in the absence of nonlinearity—above, the thresholding $\{\cdot\}^+$—this model network could evince no orientation selectivity.

As a very instructive example, we specialize to the case of *feed-forward inhibition* by setting the interaction constants $C_{EE} = C_{IE} = C_{II} = 0$. These are idealizations that capture that the neuronal network is operating in a regime of very small cortico-cortical excitation ($\tilde{g}_{EE}$, $\tilde{g}_{IE} \ll \tilde{g}_{IE}$), and interpreting the term $\tilde{g}_{II}$ as primarily a normalization. In this idealized case, the inhibitory firing rate $\langle m_I \rangle_T$ is expressed directly in terms of the LGN drive:

$$\langle m_I \rangle_T = \langle f^+ \rangle_T(\Theta), \tag{23}$$

and is only a function of Θ. This case yields for the excitatory firing rate:

$$\langle m_E \rangle_T(\mathbf{x}) = \left\langle \left\{ f(\Theta(\mathbf{x}), t) - C_{EI} \int d^2\mathbf{x}' * K_{EI}(\mathbf{x}. - \mathbf{x}')\langle f^+ \rangle_T(\Theta(\mathbf{x}'))\right\}^+ \right\rangle_T. \tag{24}$$

The geometry of firing rates and orientation selectivity follows from this expression. First, the cortico-cortical inhibition, $C_{EI}K_{EI} * \langle f^+ \rangle_T$, decreases monotonically as one moves inward along the ray

$\Theta = 0$, towards the pinwheel center; that is, from right to left along the line $(x, y = 0)$, $x > 0$. Thus, by Eq. (24), $\langle m_E \rangle_T$ increases along the ray $\Theta = 0$ as the pinwheel center is approached. Crossing the center onto the ray $\Theta = \pi$, the firing rate jumps down discontinuously (while $K_{EI} * \langle f^+ \rangle_T$ is continuous at the pinwheel center, $\langle f^+ \rangle_T$ is not) and thence increases moving out along $\Theta = \pi$. These features are observed in the point-neuron and CG simulations of Fig. 3.

Now, consider excitatory CG-cells, both near and the far from the pinwheel center: in these two cases, the support of the spatial convolution in Eq. (24) relative to the spatial variation of preferred orientation, leads to the following observations:

Far from the pinwheel center: Consider $|\mathbf{x}| \gg L_{EI}$. Eq. (19) then yields

$$\int d^2\mathbf{x}' K_{EI}(\mathbf{x} - \mathbf{x}') \langle f^+ \rangle_T(\Theta(\mathbf{x}')) \simeq \langle f^+ \rangle_T(\Theta(\mathbf{x})). \tag{25}$$

Thus, the cortico-cortical inhibition in the far-field reflects directly the LGN drive, and is both selective and determined by $\Theta(\mathbf{x})$.

Near the pinwheel center: For $|\mathbf{x}| \ll L_{EI}$,

$$\begin{aligned} &\int d^2\mathbf{x}' K_{EI}(\mathbf{x} - \mathbf{x}') \langle f^+ \rangle_T(\Theta(\mathbf{x}')) \\ &\simeq \int d^2\mathbf{x}' K_{EI}(\mathbf{x}') \langle f^+ \rangle_T(\Theta(\mathbf{x}')) \\ &= \frac{1}{2\pi} \int_0^{2\pi} \langle f^+ \rangle_T(\Theta) \, d\Theta \equiv \langle f^+ \rangle_{T,\Theta}. \end{aligned} \tag{26}$$

This last identity uses the axisymmetry of the kernel $K_{EI}(\mathbf{x})$ about $\mathbf{x} = \mathbf{0}$, that K_{EI} has unit integral, and that f depends spatially only upon Θ. Thus, the near-field cortico-cortical inhibition is determined nonlocally (as an average over Θ) and is nonselective in Θ.

These two expressions show clearly that far neurons should be inhibited very differently from near neurons—with far neurons receiving inhibition from cells with only a small range of orientation angles, and near neurons receiving inhibition averaged over cells with all orientation preferences. This difference of local *vs.* global inhibition arises because only those inhibitory neurons which are spatially close to an excitatory neuron can inhibit it monosynaptically. This distance of influence is set by the axonal arbor of the inhibitory neuron and the dendritic arbor of the excitatory neuron. Far from the pinwheel center, only neurons of very similar orientation preferences lie within this circle of influence, whereas near the pinwheel center all angles of orientation preference lie within it (see Fig. 1(a)).

Inserting the above expressions into Eq. (24) produces the following expression for the firing rates of these two CG-cells:

$$\langle m_E \rangle_T(\Theta; \text{far}) \simeq \left\langle \left\{ f(\Theta, t) - C_{EI} \langle f^+ \rangle_T(\Theta) \right\}^+ \right\rangle_T \tag{27}$$

$$\langle m_E \rangle_T(\Theta; \text{near}) \simeq \left\langle \left\{ f(\Theta, t) - C_{EI} \langle f^+ \rangle_{T,\Theta} \right\}^+ \right\rangle_T. \tag{28}$$

From these formulae the mechanisms which cause the distinct spatial patterns of firing rate and orientation selectivity become apparent. Consider CG-cells both near and far from the pinwheel center, at both preferred orientation $\Theta_{pref} = 0$, and orthogonal to preferred $\Theta_{orth} = \pm\pi$. Using that

$$\langle f^+ \rangle_T(\Theta_{orth}) \leqslant \langle f^+ \rangle_{T,\Theta} \leqslant \langle f^+ \rangle_T(\Theta_{pref}), \tag{29}$$

from Eqs. (27) and (28), gives

$$\langle m_E \rangle_T(\Theta_{pref}; \text{near}) \geqslant \langle m_E \rangle_T(\Theta_{pref}; \text{far}), \tag{30}$$

and that

$$\langle m_E \rangle_T(\Theta_{orth}; \text{near}) \leqslant \langle m_E \rangle_T(\Theta_{orth}; \text{far}). \tag{31}$$

Using the monotonicity of $K_{EI} * \langle f^+ \rangle_T$, among other things, shows the further ordering

$$\begin{aligned} \langle m_E \rangle_T(\Theta_{orth}; \text{near}) &\leqslant \langle m_E \rangle_T(\Theta_{orth}; \text{far}) \\ &\leqslant \langle m_E \rangle_T(\Theta_{pref}; \text{far}) \\ &\leqslant \langle m_E \rangle_T(\Theta_{pref}; \text{near}) \end{aligned} \tag{32}$$

with $\langle m_E \rangle_T(\Theta_{pref}; \text{near})$ being the system's highest firing rate, and $\langle m_E \rangle_T(\Theta_{orth}; \text{near})$ the lowest. Again, these firing rate properties are seen in the point-neuron simulations of [32]; see Fig. 3.

Inequalities (30) and (31) together suggest that the form of inhibition near the pinwheel center underlies the sharper selectivity found there. Further, the form of the inhibitory contribution to Eq. (24) implies that these differences in near and far field selectivity should occur over a distance L_{EI} from the pinwheel center. Indeed, the dependence upon this characteristic length-scale can be demonstrated with simulations of the CG network, as shown in Fig. 9.

Thus, in this case of feed-forward inhibition, coarse-grained analysis shows precisely that neurons near pinwheel centers are more selective for orientation than those far, and that this property arises from the global inhibition averaged over Θ near the pinwheel centers—in contrast to the local inhibition in $\Theta(\mathbf{x})$ experienced by Far neurons in the cell at $\mathbf{x}$. Moreover, similar analysis shows that temporal modulations of quantities such as membrane potentials and currents are stronger far from pinwheel centers than near (see Figs. 6 and 7).

While the analysis presented here is restricted to the highly idealized case of *feedforward inhibition*, we show in [39] that it can be extended to the full *thresholded-linear* equations. Furthermore, we expect that much of this analysis survives when using more nonlinear CG systems such as Eqs. (6) and (7)—because one central analytic property used here is the monotonicities of $\mathcal{N}$ with respect to changes in excitatory and inhibitory conductance.

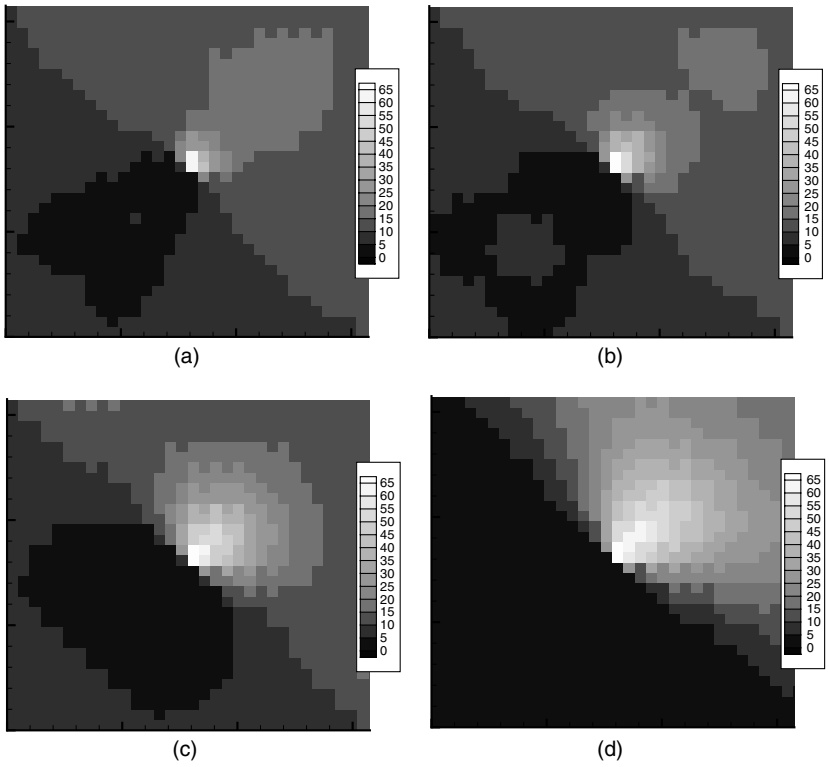

Fig. 9. From the full CG network, the spatial distribution of time-averaged excitatory firing rates for four different inhibitory coupling lengths: $L_I \approx 70$ μm (a), 100 μm (b, the standard value), 200 μm (c), and 400 μm (d).

3.3.3. ''Push–pull'' antagonism

Within our model, drifting grating stimuli produce responses for which the cortico-cortical conductances have little temporal modulation, with no ''push–pull'' antagonism between excitation and inhibition, but with a predominantly dc component to the inhibitory cortico-cortical conductance. These properties are apparent from the CG equations for drifting grating stimulus.

However, if the nonspecific, spatially isotropic coupling which introduces the phase averages is replaced by synaptic coupling which is phase selective, a ''push–pull'' antagonism can result. For example, consider a modified cortical network for which the synaptic coupling is selective for spatial phase; more specifically, with the coupling between excitatory and inhibitory neurons half-cycles out of phase. For drifting grating stimuli, this network with ''anti-phase'' selective coupling architecture takes the form

$$\begin{aligned} m_{\mathrm{E}}(\mathbf{x},t) &= \mathcal{N}_{\mathrm{E}}[\mathbf{x},t;m_{\mathrm{E}}(t),m_{\mathrm{I}}(t-T/2)] \\ m_{\mathrm{I}}(\mathbf{x},t-T/2) &= \mathcal{N}_{\mathrm{I}}[\mathbf{x},t-T/2;m_{\mathrm{E}}(t),m_{\mathrm{I}}(t-T/2)], \end{aligned} \tag{33}$$

where T is the temporal period of the drifting grating and where

$$\begin{aligned} &\mathcal{N}_{\mathrm{P}}[\mathbf{x},t;m_{\mathrm{P}}(t),m_{\mathrm{P}'}(t-T/2)] \\ &\quad = -g_{\mathrm{T,P}} \Big/ \log\left(\frac{\{I_{\mathrm{D,P}}-g_{\mathrm{T,P}}\}^{+}}{g_{\mathrm{T,P}}+\{I_{\mathrm{D,P}}-g_{\mathrm{T,P}}\}^{+}}\right) \end{aligned}$$

$$\begin{aligned} g_{\mathrm{T,E}} \equiv\ & g_{\mathrm{R}} + g_{\mathrm{lgn}}(\mathbf{x},t) + \Big(\tilde{g}_{\mathrm{EE}}[\mathbf{x},t;m_{\mathrm{E}}(t)] \\ & + \tilde{g}_{\mathrm{EI}}[\mathbf{x},t;m_{\mathrm{I}}(t-T/2)] + \bar{f}_{\mathrm{P}'}\Big) \end{aligned}$$

with analogous expressions for $g_{\mathrm{T,I}}$ and for $I_{\mathrm{D,P}}$. The cortico-cortical conductances themselves are given by

$$\begin{aligned} &\tilde{g}_{\mathrm{EE}}(\mathbf{x},t;m_{\mathrm{E}}) \\ &\quad \equiv S_{\mathrm{EE}} \int \mathrm{d}^2\mathbf{x}' \int_{-\infty}^{t} \mathrm{d}s K_{\mathrm{EE}}(\mathbf{x}-\mathbf{x}') G_{\mathrm{E}}(t-s) m_{\mathrm{E}}(s,\mathbf{x}'), \\ &\tilde{g}_{\mathrm{EI}}(\mathbf{x},t;m_{\mathrm{I}}) \\ &\quad = S_{\mathrm{EI}} \int \mathrm{d}^2\mathbf{x}' \int_{-\infty}^{t} \mathrm{d}s K_{\mathrm{EI}}(\mathbf{x}-\mathbf{x}') G_{\mathrm{I}}(t-s) m_{\mathrm{I}}(s-T/2,\mathbf{x}'), \end{aligned} \tag{34}$$

with analogous expressions for $\tilde{g}_{\mathrm{IE}}$, $\tilde{g}_{\mathrm{II}}$.

Clearly, the latter model will have inhibition in push–pull antagonism with excitation. A version of ''anti-phase selective'' synaptic coupling, combined with an orientation specific coupling architecture, is the basis of the model of [46]. The predictions for the temporal traces of the conductances (elevated dc vs. push–pull antagonism) of these two models provide distinct alternatives which clearly distinguish between these two classes of synaptic coupling schemes.

4. Discussion and conclusions

This article has provided concrete examples which illustrate how post-processing of simulational data can provide significant qualitative information about the performance of large-scale model networks—information about the models which would be difficult to obtain experimentally for real cortices, such as two-dimensional spatial distributions of cortical responses within an internal cortical layer or the time-traces of individual components of conductances. Further coarse-grained reduction of the large-scale network provide more precise information about those cortical mechanisms which underly the network's performance—analytical information, such as those relationships of regular and random cortical maps with the spatial footprints of synaptic interactions which together determine the spatial patterns of orientation selectivity.

In addition to identifying the detailed cortical mechanisms of the model network, analysis of the CG-representation can make specific predictions about the consequences of these mechanisms. For example, in a network with spatially isotropic synaptic interactions, different performance of neurons near vs. far from pinwheel centers seems typical. CG analysis can also delineate alternative mechanisms and their distinct consequences. For example, in networks with spatially isotropic synaptic connections, the broad random spatial phase distribution yields cortico-cortical conductances with little temporal modulation under drifting grating stimulation, prohibiting ''push–pull'' temporal antagonism between excitation and inhibition. On the other hand, synaptic coupling which is anti-phase specific (between excitatory and inhibitory neurons) would produce push–pull antagonism. Experiment can then check if a model's predictions occur in nature, as well as select between alternative models.

4.1. The status of experimental verification

Here we briefly summarize the status of experimental results which directly impact the responses to drifting grating stimuli described above. The anatomical and physiological experimental constraints used to construct the model are described in Section 2 and in [32]. Here we focus on experiments relevant to the predicted mechanisms of network response.

The predominance of cortical inhibition provides for many of the characteristics of Simple cell response within our model. Accurate values of in vivo conductances are extremely difficult to measure experimentally. Hence, recent experiments have focused on the demonstration of large conductance *changes* under visual stimulation [2,9,24,29]. These studies show conductance increases by factors of two to three over background values, with these increases dominated by inhibition.

Borg-Graham et al.'s [9,29] measurements indicate further that the cortico-cortical inhibition is ON-OFF as in our model. Within our model, a weakening of inhibition makes Simple cells appear to be complex, consistent with observations [21,33,42] of the consequences of weakening inhibition pharmacologically.

Regarding ''push–pull'' antagonism between excitation and inhibition, the interpretations of experimental results are somewhat contradictory at present. Some physiological studies have been interpreted to mean that there is phase-sensitive or push–pull inhibition generated intracortically [2,24]. Recent experiments of Anderson et al. [2] sought to measure Simple cell responses to drifting gratings. They report a temporal modulation of synaptic inhibition in opposition to the modulation of synaptic excitation. However, scrutiny of the measurements in [2] indicates that there usually is a large phase insensitive component of the inhibitory conductance, consistent with the phase-insensitive inhibition that is observed in our model's response to drifting gratings. Furthermore, modulation of the measured cortico-cortical inhibition was observed primarily when the cell was above threshold and firing; It is possible that their measurements of synaptic conductances were made inaccurate by the spiking. Other direct intracellular measurements by Borg-Graham and colleagues [9] indicate that inhibition in Simple cells is more often spatial phase-insensitive than phase-sensitive (or ''push–pull'')—as Borg-Graham et al. indeed noted. Further experimental measurements are clearly needed.

Our modeling work emphasizes that local synaptic coupling architectures which are spatially isotropic within the cortical layer can easily produce neuronal responses that depend upon the neuron's location relative to orientation map's pinwheel centers. For example, within our Simple cell model network, neurons in the input layer $4C\alpha$ which are near the pinwheel centers are more selective for orientation than those far (see Fig. 3).

This specific observation is only for Simple cells. But in fact, the input layer $4C\alpha$ contains approximately 50% Simple and 50% Complex cells, while other layers of V1 in macaque contain as many as 70% Complex cells [37]. Currently, we are constructing a model network which contains both Simple and Complex cells [44,45], with the Complex cell subnetwork driven more by cortico-cortical excitation (see [15]). Our preliminary results, as illustrated by Fig. 10, indicate an oppositely arranged spatial distribution for the Complex cell subpopulation. Namely, while the subpopulation of Simple cells is better tuned near the pinwheel centers, the Complex cells are better tuned away from these centers. Again, it is the interaction of the spatially isotropic synaptic couplings with the structure of the orientation preference map that produces these spatially dependent neuronal responses.

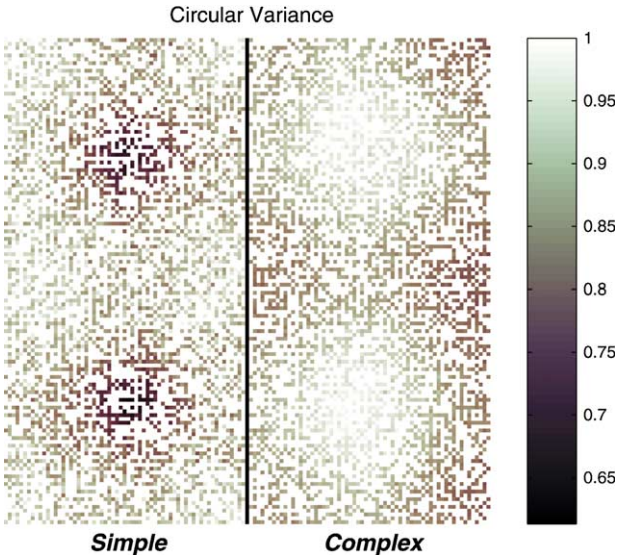

Fig. 10. A preliminary result from a cortical model which manifests both Simple and Complex cells. Across the model's four orientation hypercolumns, this shows the CVs of the Simple cells (left two hypercolumns) and Complex cells (right two hypercolumns) across the cortical surface. Note that while Simple cells are more sharply selective near the hypercolumn centers, the Complex cells are less selective.

Experimentally, such differences are just beginning to be sought. Using tetrode measurements combined with optical imaging, Maldonado et al. [31] studied experimentally whether orientation selectivity differed near and far from pinwheel centers. Using the half-width of a Gaussian fit as an estimate for orientation selectivity, they reported no substantial differences near and far from pinwheel centers. However, their study was in cat striate cortex, the laminar location of the recorded cells was unknown, and the Simple-Complex classification of these cells was not reported. Further, we have found that half-width can be fairly insensitive relative to other measures such as circular variance. Recent work from the Sur laboratory [18] does report a dependence of orientation preference plasticity upon distance from pinwheel center. Further experimental observations of responses relative to distance from pinwheel centers are definitely needed—observations which carefully monitor the neurons laminar location and cell type, as well as their distance from pinwheel centers.

Acknowledgements

The Sloan Foundation for the New York University Theoretical Neuroscience Program. National Institutes of Health Grant 2R01-EY01472. National Science Foundation Grants DMS-9971813 and DMS-9707494. The authors thank Louis Tao for useful conversations.

References

[1] J. Alonso, W. Usrey, R. Reid, Rules of connectivity between geniculate cells and simple cells in cat primary visual cortex, J. Neurosci. 21 (2001) 4002–4015.
[2] J.S. Anderson, M. Carandini, D. Ferster, Orientation tuning of input conductance, excitation, and inhibition in cat primary visual cortex, J. Neurophysiol. 84 (2000) 909–926.
[3] R. Azouz, C.M. Gray, L.G. Nowak, D.A. McCormick, Physiological properties of inhibitory interneurons in cat striate cortex, Cereb. Cortex (1997) 534–545.
[4] R. Ben-Yishai, R. Bar-Or, H. Sompolinsky, Theory of orientation tuning in the visual cortex, Proc. Natl. Acad. Sci. USA 92 (1995) 3844–3848.
[5] E. Benardete, E. Kaplan, The dynamics of primate M retinal ganglion cells, Vis. Neurosci. 16 (1999) 355–368.
[6] G. Blasdel, Differential imaging of ocular dominance and orientation selectivity in monkey striate cortex, J. Neurosci. 12 (1992) 3115–3138.
[7] G. Blasdel, Orientation selectivity, preference, and continuity in the monkey striate cortex, J. Neurosci. 12 (1992) 3139–3161.
[8] T. Bonhoeffer, A. Grinvald, Iso-orientation domains in cat visual cortex are arranged in pinwheel like patterns, Nature 353 (1991) 429–431.
[9] L. Borg-Graham, C. Monier, Y. Fregnac, Visual input evokes transient and strong shunting inhibition in visual cortical neurons, Nature 393 (1998) 369–373.
[10] W. Bosking, Y. Zhang, B. Schofield, D. Fitzpatrick, Orientation selectivity and the arrangement of horizontal connections in tree shrew striate cortex, J. Neurosci. 17 (1996) 2112–2127.
[11] P. Bressloff, J. Cowan, M. Golubitsky, P. Thomas, M. Wiener, Geometric visual hallucinations euclidean symmetry and the functional architecture of striate cortex, Philos. Trans. Royal Soc. London Ser. B 356 (2001) 299–330.
[12] P. Buzas, U. Eysel, P. Adorjan, Z. Kisvarday, Axonal topography of cortical basket cells in relation to orientation, direction, and ocular dominance maps, J. Compar. Neurol. 437 (2001) 259–285.
[13] E. Callaway, Local circuits in primary visual cortex of the macaque monkey, Ann. Rev. Neurosci. 21 (1998) 47–74.
[14] E. Callaway, A. Wiser, Contributions of individual layer 2 to 5 spiny neurons to local circuits in macaque primary visual cortex, Vis. Neurosci. 13 (1996) 907–922.
[15] F. Chance, S. Nelson, L.F. Abbott, Complex cells as cortically amplified simple cells, Nature Neurosci. 2 (1999) 277–282.
[16] R. De Valois, D. Albrecht, L. Thorell, Spatial frequency selectivity of cells in macaque visual cortex, Vision Res. 22 (1982) 545–559.
[17] G. DeAngelis, R. Ghose, I. Ohzawa, R. Freeman, Functional micro-organization of primary visual cortex: receptive field analysis of nearby neurons, J. Neurosci. 19 (1999) 4046–4064.
[18] V. Dragoi, M. Sur, Inhomogeneities in the structure of v1 orientation maps and their consequences for cortical function, Society of Neuroscience Abstracts, p. 619.
[19] D. Ferster, S. Chung, H. Wheat, Orientation selectivity of thalamic input to simple cells of cat visual cortex, Nature 380 (1996) 249–252.
[20] D. Fitzpatrick, J. Lund, G. Blasdel, Intrinsic connections of macaque striate cortex Afferent and efferent connections of lamina 4C, J. Neurosci. 5 (1985) 3329–3349.
[21] Y. Frégnac, D. Shulz, Activity-dependent regulation of receptive field properties of cat area 17 by supervised Hebbian learning, J. Neurobiol. 41 (1) (1999) 69–82.
[22] J. Gibson, M. Beierlein, B. Connors, Two networks of electrically coupled inhibitory neurons in neocortex, Nature 402 (1999) 75–79.

[23] D. Hansel, G. Mato, C. Meunier, L. Neltner, Numerical simulations of integrate-and-fire neural networks, Neural Comp. 10 (1998) 467–483.
[24] J. Hirsch, J.M. Alonso, R. Reid, L. Martinez, Synaptic integration in striate cortical simple cells, J. Neurosci. 15 (1998) 9517–9528.
[25] D. Hubel, T. Wiesel, Receptive fields, binocular interaction and functional architecture of the cat's visual cortex, J. Physiol. (London) 160 (1962) 106–154.
[26] D. Hubel, T. Wiesel, Receptive fields and functional architecture of the monkey striate cortex, J. Physiol. (London) 195 (1968) 215–243.
[27] B. Jagadeesh, H. Wheat, L. Kontsevich, C. Tyler, D. Ferster, Direction selectivity of synaptic potentials in simple cells of the cat visual cortex, J. Neurophysiol. 78 (1997) 2772–2789.
[28] C. Koch, Biophysics of Computation, Oxford University Press, Oxford, 1999.
[29] C. Monier, L. Borg-Graham, Y. Fregnac, Voltage-clamp measurement of visually-evoked conductances with whole-cell patch recordings in primary visual cortex, J. Physiol. Paris 90 (1996) 185–188.
[30] J.S. Lund, Local circuit neurons of macaque monkey striate cortex: neurons of laminae 4C and 5A, J. Compar. Neurol. 257 (1987) 60–92.
[31] P. Maldonado, I. Godecke, C. Gray, T. Bonhoeffer, Orientation selectivity in pinwheel centers in cat striate cortex, Science 276 (1997) 1551–1555.
[32] D. McLaughlin, R. Shapley, M. Shelley, J. Wielaard, A neuronal network model of macaque primary visual cortex (V1): orientation selectivity and dynamics in the input layer $4C\alpha$, Proc. Natl. Acad. Sci. USA 97 (2000) 8087–8092.
[33] A. Murthy, A.L. Humphrey, Inhibitory contributions to spatio-temporal receptive-field structure and direction selectivity in simple cells of cat area 17, J. Neurophysiol. 81 (1999) 1212–1224.
[34] A. Omurtag, B. Knight, E. Kaplan, L. Sirovich, Invest. Ophthalmol. Vis. Sci. 40 (1999) S3018.
[35] R.C. Reid, J.M. Alonso, Specificity of monosynaptic connections from thalamus to visual cortex, Nature 378 (1995) 281–284.
[36] D. Ringach, M. Hawken, R. Shapley, Dynamics of orientation tuning in macaque primary visual cortex, Nature 387 (1997) 281–284.
[37] D. Ringach, R. Shapley, M. Hawken, Diversity and laminar dependence of orientation selectivity in simple and complex cells of macaque v1, J. Neurosci. 22 (2002) 5639–5651.
[38] R. Shapley, C. Reid, Unpublished private communication, 1998.
[39] M. Shelley, D. McLaughlin, Coarse-grained reduction and analysis of a network model of cortical response. I. Drifting grating stimuli, J. Comp. Neurosci. 12 (2002) 97–122.
[40] M. Shelley, D. McLaughlin, R. Shapley, J. Wielaard, States of high conductance in a large-scale model of the visual cortex, J. Comp. Neurosci. 13 (2002) 93–109.
[41] M. Shelley, L. Tao, Efficient and accurate time-integration schemes for integrate-and-fire neuronal networks, J. Comp. Neurosci. 11 (2001) 111–119.
[42] A.M. Sillito, The contribution of inhibitory mechanisms to the receptive field properties of neurones in the striate cortex of the cat, J. Physiol. (London) (1974) 305–329.
[43] H. Sompolinsky, R. Shapley, New perspectives on the mechanisms for orientation selectivity, Curr. Opin. Neurobiol. 7 (1997) 514–522.
[44] L. Tao, M. Shelley, D. McLaughlin, R. Shapley, An Egalitarian network model for the emergence of simple and complex cells in visual cortex. Proc. Nat. Acad. Sci. USA (2003) in press.
[45] L. Tao, M. Shelley, D. McLaughlin, R. Shapley, How complex cells are made in a simple cell network, presented Society for Neuroscience, 2001.
[46] T. Troyer, A. Krukowski, N. Priebe, K. Miller, Contrast invariant orientation tuning in cat visual cortex with feedforward tuning and correlation based intracortical connectivity, J. Neurosci. 18 (1998) 5908–5927.
[47] J. Wielaard, M. Shelley, R. Shapley, D. McLaughlin, How Simple cells are made in a nonlinear network model of the visual cortex, J. Neurosci. 21 (14) (2001).
[48] H. Wilson, J. Cowan, A mathematical theory of the functional dynamics of cortical and thalamic nervous tissue, Kybernetik 13 (1973) 55–80.
[49] T. Yousef, T. Bonhoeffer, D. Kim, U. Eysel, E. Toth, Z. Kisvarday, Orientation topography of layer 4 lateral networks revealed by optical imaging in car visual cortex (area 18), Eur. J. Neurosci. 11 (1999) 4291–4308.